nature climate change

SUPPLEMENTARY INFORMATION

DOI: 10.1038/NCLIMATE2658

# Projected strengthening of Amazonian dry season by constrained climate model simulations

Juan P. Boisier*, Philippe Ciais, Agnès Ducharne and Matthieu Guimberteau

*Corresponding author address:

Juan Pablo Boisier

Department of Geophysics, Universidad de Chile, Santiago, Chile

jboisier@dgf.uchile.cl

# 1 CMIP5 model data

The Coupled Model Intercomparison Project Phase 5 (CMIP5) coordinates a large number of modelling experiments designed for the assessment of climate change[1]. The anthropogenic climate forcing (ACF) accounted for in CMIP5 includes changes in atmospheric concentration of long-lived — greenhouse — gases, short-lived gases and aerosols, as well as changes in land-use. In this study, we analyze transient fully-forced simulations of the historical period (1960–2005) and of the 21st century (2006–2099) following the Representative Concentration Pathway 8.5 (RCP8.5). RCP8.5 represents the most pessimistic socioeconomic/climate policy scenario currently assessed in CMIP5[2]. It prevails no mitigation efforts in the use of fossil fuels and an underlying radiative forcing of around 8.5 W $m^{-2}$ in 2100 with respect to preindustral conditions. In the same period, the multi-model projections show an increase in global temperature of $\sim 4.5 \pm 1.5$°C.

We use a single pair of runs (historical and RCP8.5) from 36 GCMs participating in CMIP5 (Table S1). The model data analyzed include monthly precipitation and sea-level pressure ($p_{SL}$) fields. Vertically integrated moisture fluxes were also computed (see Methods' section in main text) for a subset of models for which three-dimensional fields of wind and specific humidity were available at the time of this study (all GCMs assessed excepting bcc-csm1-1, bcc-csm1-1-m, EC-EARTH, FGOALS-s2 and HadGEM2-AO).

# 2 Precipitation data sets: uncertainties and historical rainfall trends in Amazonia

Four data sets of land precipitation were used in this study: the Global Precipitation Climatology Center Full Re-Analysis Version 6 (GPCC; ref. 3), the NOAA/CPC Monthly Global Precipitation Reconstruction over Land (PREC/L, ref. 4), the Climate Research Unit Time-Series (TS) Version 3.21 Precipitation (CRU, ref. 5) and the University of

Delaware Terrestrial Precipitation Version 3.02 (UDEL, ref. 6). All of them are widely used global products based on long-term gauge observations, available in grids of 0.5° or coarser resolution, at monthly time steps and, for the versions used, updated up to 2010 or 2012. In the GPCC case, we extended the data set until 2012 with the GPCC Monitoring Product Version 4. A preliminary evaluation of both GPCC products indicated almost no precipitation biases between them across Amazonia during the overlapping period (2007–2010).

The four products differ in the input database, and in the filtering and gridding technique applied. GPCC is probably the most reliable long-term (prior to 1980) and gridded precipitation data set based on surface observations, because of the large number of stations analyzed, the strict quality controls and the evaluation/update frequency. However, given the scarcity of historical precipitation observations across Amazonia, we favoured a multi-product approach to account for the observational uncertainties. There are, indeed, important differences between the products within the domain of study (Fig. S1). Beside some biases in western Amazonia, there is a general agreement in the climatological mean rainfall values. Yet, clear differences are observed in the month-to-month covariability, with typical error values (RMSE) above 2 mm $d^{-1}$ in many regions within the Amazon basin. Using GPCC as a reference, the strongest errors are found in the CRU data set, notably in western areas of the basin that show RMSE values up to 4 mm $d^{-1}$.

The Amazonian precipitation ($P_A$) uncertainties can be seen more clearly when the slow variations and trends are compared across the products (Fig. S2). There is a general agreement in the basin-wide mean $P_A$ interannual variability, but differences are manifest in decadal variations (Fig. S2a). All the products indicate a relative wet period during the 1970s and a positive trend since the mid-1990s. CRU shows a particular dry period in the 1980s and a strong wet trend since then.

The linear trends indicate a similar seasonal pattern between the four data sets, but the amplitudes are largely product-dependent. As shown in Fig. 2b (replotted in Fig. S2b), the trends of $P_A$ computed between 1960 and 2010 show positive values during the wet

season (December-February) and a drying signal in late dry season (July to November). The end-of-dry-season $P_A$ decline and a concomitant dry-season lengthening is systematic over different periods, but the amplitude of this trend is particularly large since the 1970s (Fig. S2c) and 1980s (Fig. S2d). In contrast, the wet trend in January-June is a more recent behaviour.

The 1980–2010 $P_A$ trends reveal important discrepancies between the data sets. In, e.g., February or May, the trends show a range between the products exceeding 3 mm $d^{-1}$ per century (Fig. S2d). A particularly large rainfall increase is derived from CRU in the first part of the year. Given these differences, we also look at the evolution of the River Amazon discharge (RD) observed since the late 1960s at Óbidos[7]. We note that the Amazon basin domain used in this study is larger than the catchment area and associated streamflow measured at Óbidos, which does not include the Rio Tapajs and Rio Xingu catchments, nor other regions on the eastern margin of Brazilian Amazonia. However, most precipitation across the domain of study drains through the sub-basins flowing past the Óbidos station. The annual RD at this station shows, indeed, a fairly good correlation with the basin-wide mean $P_A$ time-series obtained with the products (Fig. 2a).

Considering the lag of around one season that the runoff from the various Amazon sub-basins takes to reach Óbidos[8] (see inset in Fig. S2c), the seasonal pattern of the Amazon RD trends matches fairly well the general picture shown by the precipitation data. Coherent with the end-of-dry-season precipitation decline, negative RD trends are observed at the end of the year in both periods 1970–2010 (Figs. S2c) and 1980–2010 (Figs. S2d). As previously reported[9], the most recent period indicates a pronounced positive RD trend during most of the year, also in agreement with the positive $P_A$ trend observed in January-June.

These results indicate that despite some clear discrepancies between the precipitation products in Amazonia, robust historical variations in the Amazonian hydrology can be inferred from them. As discussed in the main text, the seasonality of the long-term (1960–2010) $P_A$ trends show a general agreement with the modelled trends during the

same period and across the 21st century (Fig. 2 in main text). However, given the large variability in tropical South America and the observational uncertainties in this region, to distinguish transient — human-induced — changes in the South American Monsoon from its natural variations is clearly not a simple task. A proper detection and attribution of the current hydrological trends in Amazonia remain, hence, a challenge.

# 3 Amazonian precipitation and large-scale circulation relationship

The main result presented in this study is based on $P_A$ projections that combine simulated (GCM) and observational data. The approach we follow relies on the major influence the circulation changes have on the precipitation variability. Among other factors, we consider that the GCM $P_A$ projections depend on mesoscale rainfall (Amazonia) sensitivities to changes in large-scale motion — a feature we try to constrain using observational data (see Fig. 1b in main text).

The covariability between $p_{SL}$ over different regions of the globe and $P_A$ evidences those model-specific sensitivities. The interannual correlation between $p_{SL}$ and $P_A$ (basin-wide mean), computed with an observational data set and with two CMIP5 GCMs, is illustrated in Fig. S3. In January, the first case indicates positive and negative values over the East and West Pacific Ocean, respectively (Fig. S3a). The atmospheric signature of El Niño–Southern Oscillation (ENSO) can be recognized on this pattern, reflecting the major influence that ENSO exerts on the tropical South American precipitation during the wet season (see ref. 10 and references therein). The corresponding correlation map derived with CanESM2 indicates a similar behavior (ENSO-like) in January, but the modeled link between $P_A$ and this global phenomena is strongest than the one obtained with the observational products. In contrast, the MPI-ESM-MR correlation map does not show such a relation nor a clear pattern across the Pacific Ocean. The signals of

covariability between $P_A$ and $p_{SL}$ are weaker in July compared to those in January, and there is no clear consistency between the GCMs assessed and the observations. The moderate negative correlation between $P_A$ and $p_{SL}$ over the tropical Atlantic is likely the most systematic signal across GCMs, the observations and seasons.

The GCM-based correlation maps shown in Fig. S3 illustrate how different the modeled relationship between $P_A$ and the large-scale circulation could be. These two models were chosen as examples because the associated empirical $P_A$ models (described next) show the largest (CanESM2) and weaker (MPI-ESM-MR) capacity to reproduce the simulated $P_A$ (Fig. S7). We note that this capacity does not necessarily indicate that the $P_A$ regime simulated by a given GCM is closer to the real word, but just a stronger influence of the large-scale $p_{SL}$ on $P_A$.

## Amazonian precipitation models computation and evaluation

The methodology followed both to derive the constrained $P_A$ projections and to evaluate this approach is summarized in Fig. S4. We make use of regression models of $P_A$ calibrated with four observational data sets of precipitation (described in Section 1) and one of $p_{SL}$ (based on HadSLP2; see methods' section in main text), which is used to derive a number of explanatory variables. To obtain the diagnostic ensemble of $P_A$ projections, these models are then forced with the $p_{SL}$ simulated by the CMIP5 GCMs from 1960 to 2099.

As we note in the main text, a number of different processes that could influence the present-day and long-term $P_A$ variability are not considered here. Hence, we do not have an a priori confidence that the simple empirical precipitation models calibrated with historical data are capable of predicting the 21st century evolution of $P_A$. To evaluate this, we computed another set of models based on the historical $P_A$ and $p_{SL}$ data simulated

by each CMIP5 GCM (Fig. S4). The future $P_A$ changes simulated by the CMIP5 GCMs are considered as different 'realities' against which we can test our simple models. An important assumption should be noted here: this evaluation considers that if the method works for these different GCMs, then it should also work for the real word.

A first step in the method includes the statistical decomposition of $P_A$. The spatio-temporal rainfall variability across the Amazon basin is represented by the leading 10 modes resulting from a standard Empirical Orthogonal Function (EOF) analysis. The first concern of using EOF is whether the leading modes of precipitation describing the historical variability (1960–2012) are able to well represent the future patterns of change in response to ACF. To evaluate this, we first projected for each GCM the rainfall fields simulated from 1960 and 2099 onto the corresponding EOFs computed from 1960 to 2012. The resultant long-term (1960–2099) Principal Components (PCs) associated with the 10 leading modes are then used to reconstruct the $P_A$ fields for the whole period. Fig. S5 illustrates the $P_A$ changes between the ends of the 20th and 21st centuries ($\Delta P_A$) simulated by the GCMs and those obtained with the EOF-projected (reconstructed) fields. On average across the GCMs, the spatial and seasonal patterns of change are well-captured by the reconstructions. The basin-wide mean annual $P_A$ from 1960 to 2099 that resulted from them is also plotted separately for each GCM in Fig. S6 (red lines), indicating almost no difference with the simulated time-series (black lines).

Given that the modes characterizing the historical precipitation variability in Amazonia also serve to describe the future projections, we use the PC time-series as predictands in the regression computations. This approach is more efficient than performing multiple analyses on the precipitation data of single grid-cells, and ensures a spatial consistency on the reconstructed precipitation fields.

Excepting the analysis based on the UDEL precipitation product (which is updated until 2010), all the observations and GCM-based regression models were calibrated with the 53-years period spanning from 1960 to 2012. As is briefly described in the main methods section, the analyses were performed for each month separately, but including

neighbouring months each time. Hence, the model calibration accounts for interannual and part of the seasonal variability. A stepwise multilinear regression was adopted to select a subset of potential predictors of large-scale circulation, which correspond to normalized anomalies of $p_{SL}$ averaged in a global grid of 20° latitude-longitude. An automatic procedure adds and removes terms (single grid-cell $p_{SL}$ anomalies) in the model until a criterion of statistical significance is satisfied (a p-value threshold of 0.05). The final model obtained avoids overfitting maintaining high predictive performance, but depends on an initial set of predictors. We therefore randomly select a set of initial conditions to perform an ensemble of 50 different models. The mean response from each ensemble was finally used both for the method evaluation and to derive the constrained $P_A$ projections. Preliminary tests indicate no significant differences in the ensemble mean response including a larger number of realizations.

Considering the relative simplicity of the empirical models constructed, they show a fairly good capacity to reproduce the observed and simulated $P_A$. The statistical predictions explain most of the interannual variability (Fig. S7a) and trends (Fig. S7b) of $P_A$ during the historical (calibrating) period. The fraction of $P_A$ variance explained by the models derived with observations is similar — higher in some cases — than that shown by the GCM-based models (Fig. S7a). This is somewhat surprising considering that, unlike the GCMs that are internally consistent, the precipitation and $p_{SL}$ data sets adopted are independent and, as described above, prone to a number of uncertainties.

Of further interest regarding the purpose of this study is the empirical models' skill to predict the future evolution of $P_A$. The sign of the annual $\Delta P_A$ simulated by the GCMs is in most cases predicted by the corresponding (GCM-based) empirical model (Fig. S7c). The statistically predicted time-series of annual basin-wide mean $P_A$ are also illustrated for each GCM in Fig. S6. The simulated $P_A$ (black curves in Fig. S6) are plotted along with the ones resulted from the corresponding regression model (grey). The interannual variations and long-term $P_A$ changes are well-predicted in most GCMs, with some remarkable cases such as ACCESS1-3, bcc-csm1-1-m, FGOALS-g2, GFDL-

CM3, GFDL-ESM2G or the three IPSL model versions. For some GCMs, however, the predicted change of $P_A$ at the end of the 21st century does not match the simulated one. This is particularly the case for the CMCC GCMs and for FIO-ESM. The seasonal details of the ensemble-mean GCM projections are also well-reproduced by empirical models, as is shown for the basin-wide averages in Fig. 2f (main text). The regional patterns of the predicted $\Delta P_A$ are generally well-predicted, although the rainfall reduction in the northeast part of the basin is slightly underestimated in SON (Fig. S5c).

# References


1. Taylor, K. E., Stouffer, R. J. & Meehl, G. A. An overview of CMIP5 and the experiment design. Bull. Am. Meteorol. Soc. 93, 485–498 (2011).

2. Moss, R. H. et al. The next generation of scenarios for climate change research and assessment. Nature 463, 747–756 (2010).

3. Rudolf, B., Becker, A., Schneider, U., Meyer-Christoffer, A., & Ziese, M. GPCC Status Report December 2010, Global Precipitation Climatology Centre – GPCC, Offenbach, Germany, 7 pp., (2010).

4. Chen, M., Xie, P., Janowiak, J. E. & Arkin, P. A. Global land precipitation: A 50-yr monthly analysis based on gauge observations. J. Hydrometeorol. 3, 249–266 (2002).

5. Harris, I., Jones, P. D., Osborn, T. J. & Lister, D. H. Updated high-resolution grids of monthly climatic observations — the CRU TS3.10 Dataset. Int. J. Clim. 34, 623–642 (2014).

6. Willmott and Matsuura. Terrestrial Precipitation Time Series (1900–2010) Version 3.02. (2012).

7. Cochonneau G. et al. The environmental observation and research project, ORE HYBAM, and the rivers of the Amazon basin, in Climate Variability and Change—hydrological Impacts, IAHS Publication 308, 44–50, (IAHS Press, 2006).

8. Guimberteau, M. et al. Testing conceptual and physically based soil hydrology

schemes against observations for the Amazon Basin. Geosci. Model. Dev. 7, 1115–1136 (2014).

9. Gloor, M. et al. Intensification of the Amazon hydrological cycle over the last two decades. Geophys. Res. Lett. 40, 1729–1733 (2013).

10. Garreaud, R. D., Vuille, M., Compagnucci, R. & Marengo, J. Present-day South American climate. Palaeogeography, Palaeoclimatology, Palaeoecology 281, 180–195 (2009).

Table S 1: List of climate models participating in CMIP5 used in this study

| **Institution** | **Model acronym (ref. number)** |
|---|---|
| Commonwealth Scientific and Industrial Research Organization (CSIRO) and Bureau of Meteorology (BOM), Australia. | ACCESS1-0 (1), ACCESS1-3 (2) |
| Beijing Climate Center (BCC), China Meteorological Administration, China. | bcc-csm1-1 (3), bcc-csm1-1-m (4) |
| College of Global Change and Earth System Science, Beijing Normal University (BNU), China. | BNU-ESM (5) |
| Canadian Centre for Climate Modelling and Analysis (CCCMA), Canada. | CanESM2 (6) |
| National Center for Atmospheric Research (NCAR), USA. | CCSM4 (7) |
| Community Earth System Model Contributors (NSF-DOE-NCAR), USA. | CESM1-BGC (8), CESM1-CAM5 (9) |
| Centro Euro-Mediterraneo per I Cambiamenti Climatici (CMCC), Italia. | CMCC-CESM (10), CMCC-CM (11), CMCC-CMS (12) |
| Centre National de Recherches Météorologiques / Centre Européen de Recherche et Formation Avancée en Calcul Scientifique (CNRM-CERFACS), France. | CNRM-CM5-2 (13) |
| Commonwealth Scientific and Industrial Research Organization in collaboration with Queensland Climate Change Centre of Excellence (CSIRO-QCCCE), Australia. | CSIRO-Mk3-6-0 (14) |
| EC-EARTH consortium. | EC-EARTH (15) |
| LASG, Institute of Atmospheric Physics, Chinese Academy of Sciences and CESS, Tsinghua University, China. | FGOALS-g2 (16) |
| LASG, Institute of Atmospheric Physics, Chinese Academy of Sciences, China. | FGOALS-s2 (17) |
| The First Institute of Oceanography (FIO), SOA, China. | FIO-ESM (18) |
| NOAA Geophysical Fluid Dynamics Laboratory (GFDL), USA. | GFDL-CM3 (19), GFDL-ESM2G (20), GFDL-ESM2M (21) |
| NASA Goddard Institute for Space Studies (GISS), USA. | GISS-E2-H (22), GISS-E2-R (23) |
| Met Office Hadley Centre (MOHC), UK. | HadGEM2-AO (24), HadGEM2-ES (25) |
| Institute for Numerical Mathematics (INM), Russia. | Inmcm4 (26) |
| Institut Pierre-Simon Laplace (IPSL), France. | IPSL-CM5A-LR (27), IPSL-CM5A-MR (28), IPSL-CM5B-LR (29) |
| Japan Agency for Marine-Earth Science and Technology, Atmosphere and Ocean Research Institute (The University of Tokyo), and National Institute for Environmental Studies (MIROC), Japan. | MIROC5 (30), MIROC-ESM (31) |
| Max-Planck-Institut fr Meteorologie (MPI-M), Germany. | MPI-ESM-LR (32), MPI-ESM-MR (33) |
| Meteorological Research Institute (MRI), Japan. | MRI-CGCM3 (34) |
| Norwegian Climate Centre (NCC), Norway. | NorESM1-M (35), NorESM1-ME (36) |

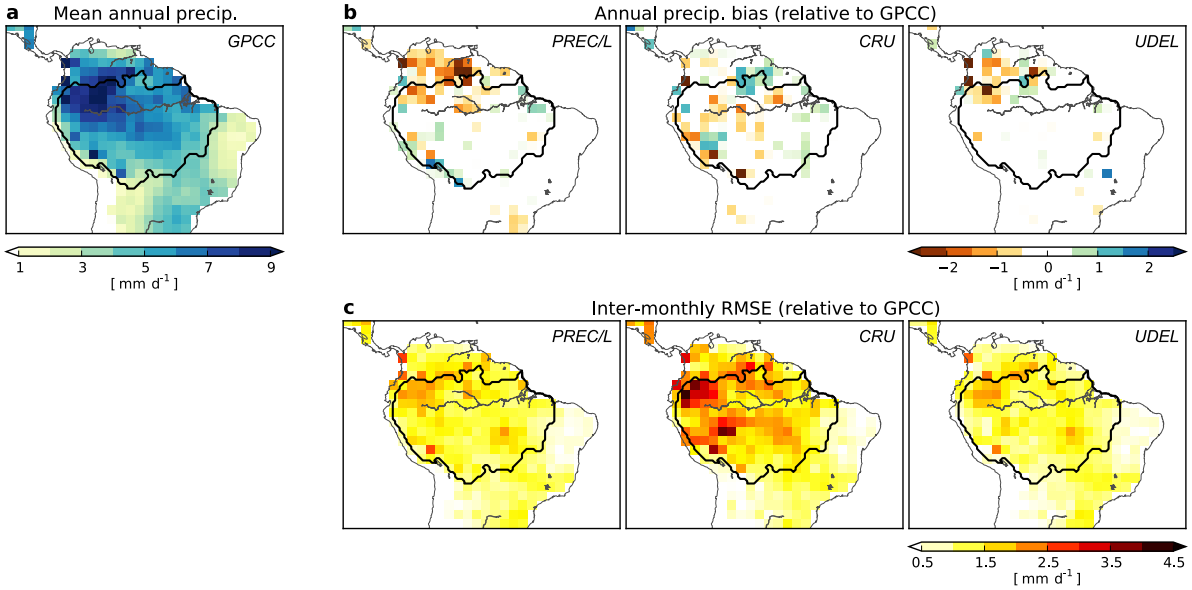


Figure S1: **Precipitation data sets comparison.** **a**, Climatological mean (1960–2010) annual precipitation from GPCC. **b**, Annual mean precipitation bias computed for the various products of precipitation assessed with respect to GPCC. **c**, Root-mean-square error (RMSE) computed between the monthly time-series (1960–2010) of the various precipitation products and GPCC.

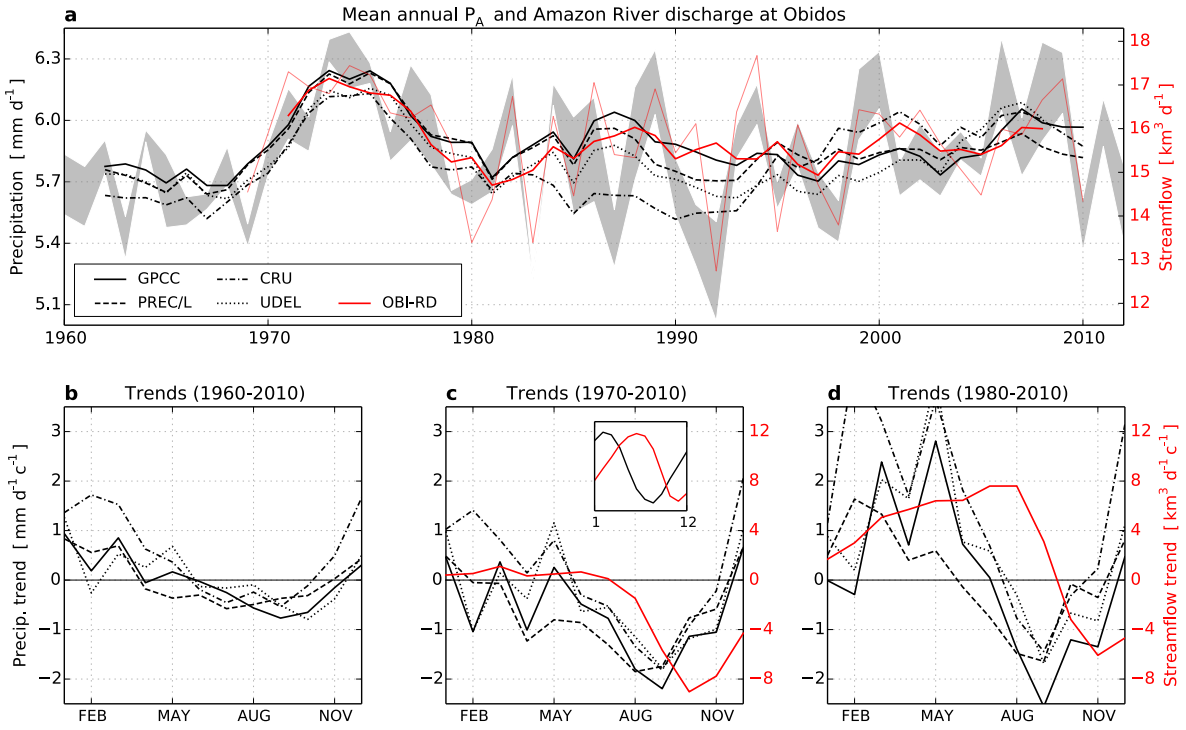


Figure S2: **Amazon basin precipitation and River discharge trends.** **a**, Annual mean precipitation in Amazonia ($P_A$, basin-wide mean) obtained with the four products used in this study (see legend). Grey envelope indicates the yearly rainfall range between the products. Thin-red curve shows the annual River Amazon discharge observed at Óbidos (OBI-RD). Thicks lines indicate the individual time-series of $P_A$ (black) and OBI-RD (red) smoothed with a 5-year running mean filter. **c**–**d**, Linear trends of $P_A$ and of OBI-RD deduced from the various data sets for different periods: 1960–2010 (**b**), 1970–2010 (**c**) and 1980–2010 (**d**). Inset in panel **c** illustrates the seasonal cycle delay of OBI-RD (red) with respect to $P_A$ (black).

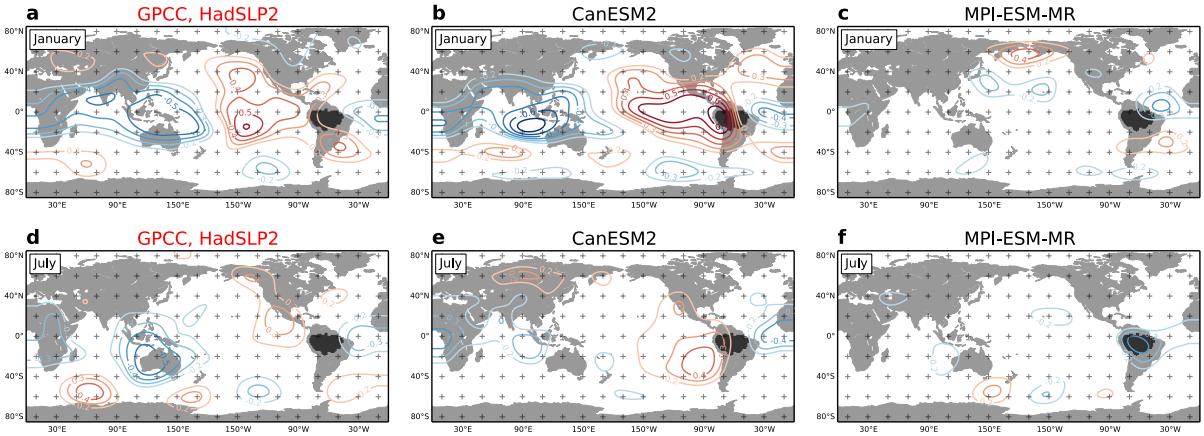


Figure S3: **Amazonian precipitation and global sea-level pressure covariability.** Correlation coefficient computed at interannual time-scales (1960–2010) between precipitation in Amazonia (basin-wide mean) and sea-level pressure ($p_{SL}$) at different locations of the globe. Maps show the analysis for January (**a**–**c**) and July (**d**–**f**) computed with an observational data set (GPCC for precipitation and HadSLP2 for $p_{SL}$) (**a**, **d**), with CanESM2 (**b**, **e**), and with MPI-ESM-MR (**c**, **f**). Plus marks indicate the grid (20° latitude-longitude) used for $p_{SL}$ in the present analysis and used further to set the explanatory variables in the regression models computation.

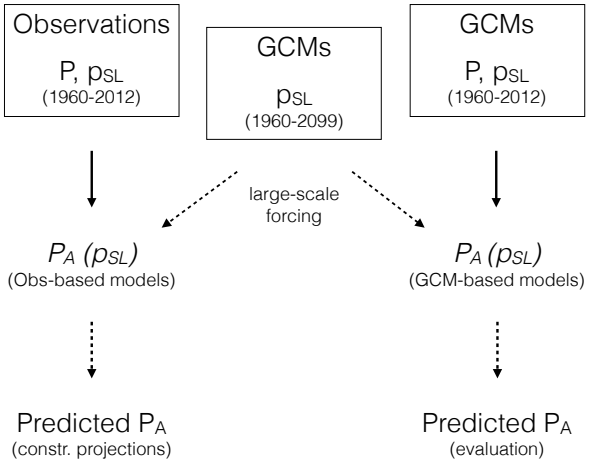


Figure S4: **Method summary.** Flowchart of the procedure followed both to derive the constrained Amazonian precipitation ($P_A$) projections and to evaluate this approach. Precipitation (P) and sea-level pressure ($p_{SL}$) input data (boxes) from observational products and GCMs are used to calibrate (solid arrows) or to force (dashed arrows) regression $P_A$ models.

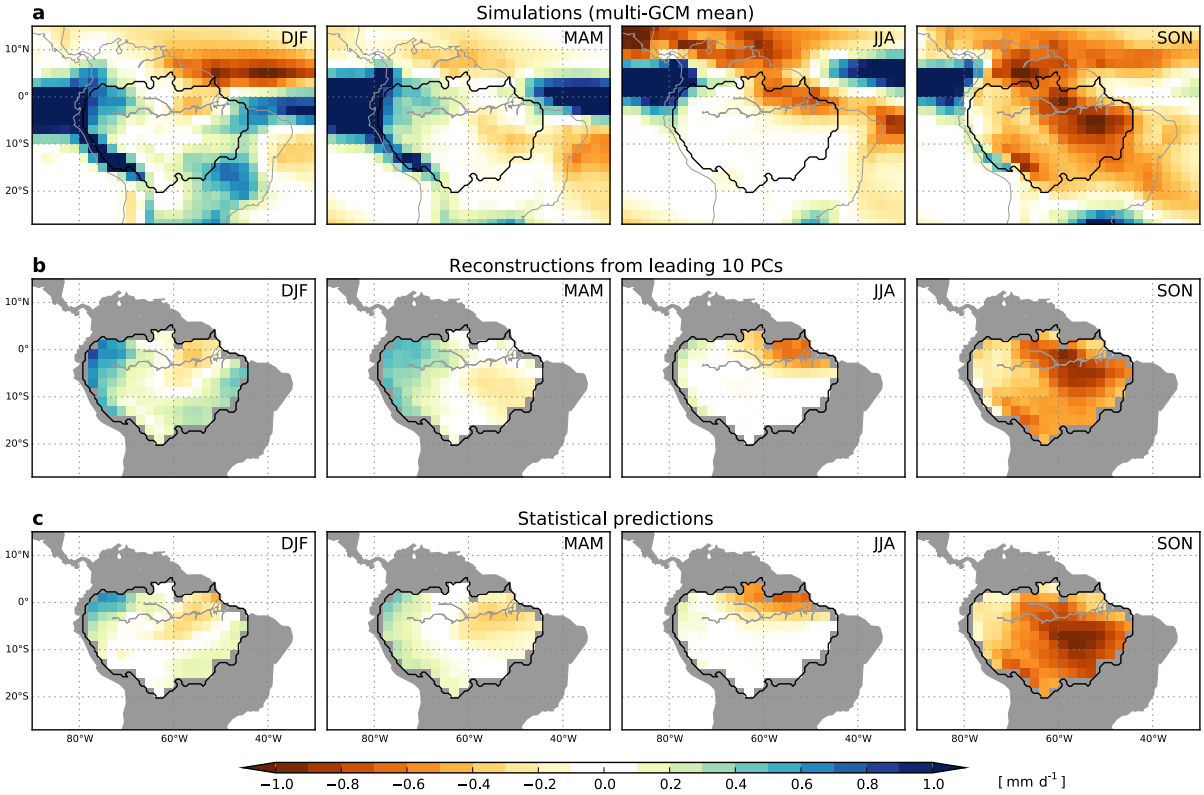


Figure S5: **Long-term precipitation changes.** Seasonal and ensemble mean precipitation difference between the ends of 20th (1960–1999) and 21st (2060–2099) centuries simulated with the CMIP5 GCMs (**a**), reconstructed with the leading 10 EOFs (**b**) and statistically predicted with GCM-based regression models (**c**).

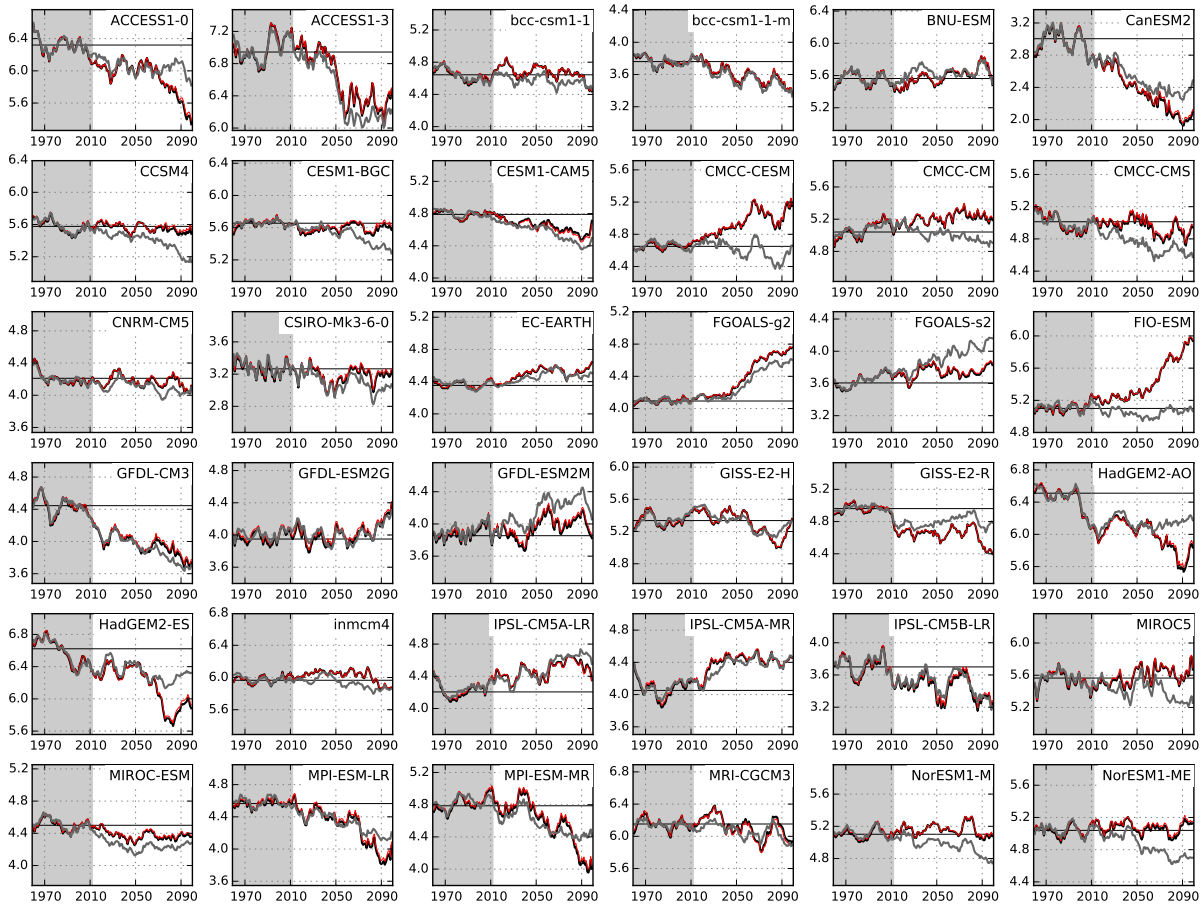


Figure S6: **Simulated, reconstructed and predicted precipitation in Amazonia.** Annual precipitation, averaged across the Amazon basin, simulated by 36 CMIP5 GCMs (black line), reconstructed with the leading 10 principal components (red) and statistically predicted (grey) from 1960 to 2099. All time series are smoothed with an 11-yr running mean filter. Grey area indicates the period used to calibrate the empirical precipitation models.

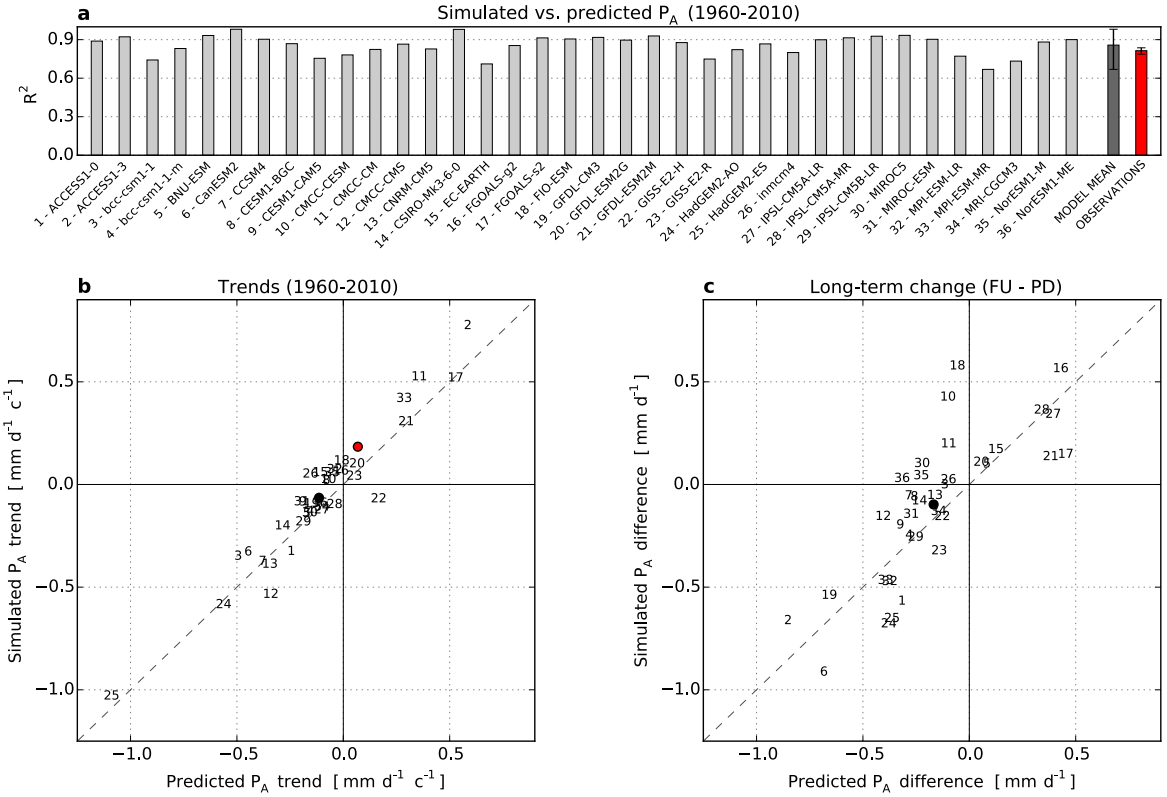


Figure S7: **Empirical models evaluation.** **a**, Simulated (GCM) annual precipitation in Amazonia ($P_A$, basin-wide mean) vs. predicted $P_A$ (GCM-based regression model) coefficient of determination ($R^2$) computed from 1960 to 2010 (light-gray boxes). Black and red boxes (error bars) indicate, respectively, the mean $R^2$ (range) obtained with the GCM-based and with the observation-based models. **b**, Scatter plot between the basin-wide mean annual $P_A$ trends (1960–2010) predicted and simulated. Numbers indicate the various GCMs assessed (see panel **a**). Black and red circles show the average trends resulted from the GCMs and the observations, respectively. **c**, As in (**b**) but for precipitation change between the ends of the 21st (2060–2099) and the 20th (1960–1999) centuries.